Microfluid Nanofluid (2016) 20:55
DOI 10.1007/s10404-016-1720-7

RESEARCH PAPER

Separation of highly viscous fluid threads in branching microchannels

Thomas Cubaud[1] · Diane Henderson[1] · Xiaoyi Hu[1]

Received: 20 October 2015 / Accepted: 17 February 2016
© Springer-Verlag Berlin Heidelberg 2016

Abstract We experimentally study the transport properties of threads made of high-viscosity fluids flowing in a sheath of miscible, low-viscosity fluids in bifurcating microchannels. A viscous filament is generated using a square hydrodynamic focusing section by injecting a 'thick' fluid into the central channel and a 'thin' fluid from the side channels. This method allows us to produce miscible fluid threads of various sizes and lateral positions in a straight channel and enables the systematic study of the downstream thread's response to flow partitioning in branching microfluidic networks at low Reynolds numbers. A phase diagram detailing the various flow patterns observed at the first bifurcation, including thread folding, transport, and fouling, is presented along with transition lines. We also examine the role of viscous buckling instabilities on thread behavior and the formation of complex viscous mixtures and stratifications at the small scale. This work shows the possibility to finely control thread trajectory and stability as well as manipulate the structural arrangement of high-viscosity multiphase flows in complex microfluidic systems.

Keywords Multiphase flow · Miscible fluids · Flow pattern · Viscous folding · Stratification · Fluidic network · Hydrodynamics instability

✉ Thomas Cubaud
thomas.cubaud@stonybrook.edu

[1] Department of Mechanical Engineering, Stony Brook University, Stony Brook, NY 11794-2300, USA

1 Introduction

Branching channels are widespread in nature and across a range of scales, from leaf venation and bronchioles in the lungs to distributary channels in river deltas. In general, splitting flows into multiple channels is practical for the transport and distribution of fluids over large areas and typically occurs through a complex system of ramification channels that can evolve over time. Separating streams is also common in chemical plants, where branched pipelining is used for flow management and directing fluids into specific reactors (Couper et al. 2005). In the case of dispersed phase flows involving components such as solid particulates, gas bubbles, or liquid droplets, bifurcating microchannels are pivotal to separation processes and offer the possibility to filtrate, dilute, or concentrate constituents using a variety of techniques (Lenshof and Laurell 2010; Hardt and Hahn 2012; Brouzes et al. 2015). A fine tuning between flow rates, fluid properties, and branching geometries can also be employed to manipulate the size of droplets or bubbles in microfluidic platforms (Link et al. 2004; Ménétrier-Deremble and Tabeling 2006; Jullien et al. 2009; Leshansky et al. 2012). In this context, the subtle interaction between size and concentration of fluid particles with flow rate in each branch has been extensively studied (Engl et al. 2005; Pozrikidis 2012; Parthiban and Khan 2013).

In contrast to the situation of dispersed flows, the dynamics of viscous separated flows has been relatively unexplored in bifurcating microchannels (Barnett and Cochrane 1956; Engl et al. 2006). The ability of high-viscosity fluids to stratify and form threads surrounded with low-viscosity fluids in confined geometries due to self-lubrication effects (Joseph et al. 1984) and curved interfaces (Guillot et al. 2006), however, opens opportunities for the development of methods to handle and mix a range of

Published online: 19 March 2016

thick and reactive substances at the small scale. The simple microfluidic design of branching channels is advantageous for manipulating local concentrations and interfacial area of multiphase flows. As the flow of viscosity-differing fluids can spatially evolve and form complex structures over short distances (Cao et al. 2003; Xia et al. 2010; Cubaud and Notaro 2014), predicting the distribution and mixing of viscous materials in bifurcating microgeometries presents significant challenges due to the influence of local viscosities on stream velocities as well as viscous buckling instabilities (Cubaud and Mason 2012).

Here, we investigate the transport properties of high-viscosity multiphase flows in simple distributary systems composed a dichotomous array of branching microchannels of equal size. A lubricated viscous thread is produced in a sheath of miscible, low-viscosity fluid using a focusing geometry located upstream of a main channel. Since downstream branches have similar dimensions, the flow rate in distributaries decreases after each bifurcation. This localized deceleration can induce significant flow destabilization, including thread viscous folding at the separation edge, shear-induced buckling deformation in straight channels, or thread lubrication failure (i.e., thread direct contact with solid walls) leading to the fouling of specific branches with high-viscosity fluid. In general, we examine the mechanisms at play during the distribution of viscous materials across a large microfluidic area through the study of thread dynamical response to flow partitioning and the formation of resulting complex stratifications downstream of a bifurcation. First, we inquire about the relationships between flow rates, thread size, and lateral positioning in a main straight channel for a range of viscosity contrasts. Second, we develop a phase diagram of flow regimes at the first bifurcation based on dimensionless flow parameters. Then, we conduct a close examination of the folding instability in confined geometries. Finally, we examine the peculiar evolution of threads and stratifications along the microfluidic network.

2 Experimental methods

The microfluidic system consists of a series of interconnected square microchannels of identical height $h = 250$ µm. Fluids are introduced into a symmetric hydrodynamic focusing section, which is connected to a central channel that splits into two branches with a bifurcating angle of $\pi/2$ (Fig. 1). Downstream, a succession of bifurcations having a similar angle of $\pi/2$, is applied to each branch to produce a simple dichotomous tree-like network resulting in eight terminal branches as described in Sects. 6 and 7. To insure the same flow rate in each channel, all terminal branches have the same length and

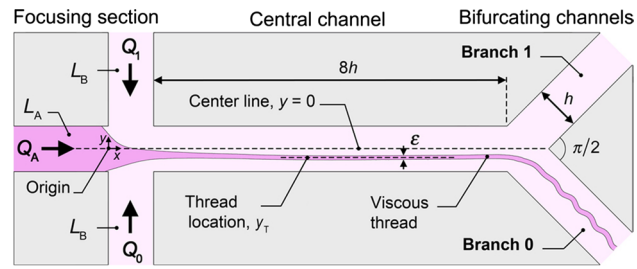

Fig. 1 Schematic of branching microchannels. All channels are square in cross section with a height of $h = 250$ µm. First part of the network includes hydrodynamic focusing section, central channel, and initially bifurcation channels

discharge into a single microfluidic pool connected to the outlet. The device is constructed using conventional silicon-based microfabrication techniques (Madou 2012), where microchannel sidewalls are etched through a silicon wafer and top and bottom walls are made of borosilicate glass sealed to the silicon slab using anodic bonding. Flexible tubes are connected to the device to inject and recover fluids, and the microdevice is placed on top of an inverted microscope equipped with a high-speed camera to record and document flow behavior.

To produce a lubricated thread, a high-viscosity fluid (L_A) is injected from the central channel at a volumetric flow rate Q_A and a low-viscosity fluid (L_B) is introduced from the side channels at flow rates Q_0 and Q_1, which are independently controlled with separate syringe pumps. The total side flow rate is labeled $Q_B = Q_0 + Q_1$. Fluids are made of conventional polydimethylsiloxane (PDMS) oils of kinetic viscosity $\nu_A = 500$ cS for L_A and various viscosities ν_B ranging from 0.65 to 10 cS for fluid L_B to examine the effects of dynamic viscosity contrasts $\chi = \eta_A/\eta_B$ of 52, 106, 180, and 990. In this work, we focus on phenomena where diffusion and inertial effects are relatively negligible on thread behavior for Péclet numbers $\mathrm{Pe} = (Q_A + Q_B)/(hD) \geq 2.4 \times 10^4$, with D being the diffusion coefficient between selected silicone oils, and Reynolds numbers $Re = (Q_A + Q_B)/(h\nu_B) \leq 21$ (Cubaud and Notaro 2014). Given the relatively low value of Re, flows are considered fully developed after a short distance $x < h$ from the fluid junction (Tritton 1988). The absolute flow rate ratio is defined as $\varphi_0 = Q_A/(Q_0 + Q_1)$. This parameter essentially controls the thread diameter ε. The thread lateral position y_T is manipulated with the ratio of the side flow rates that we label 'symmetry ratio' according to $\varphi_S = Q_0/Q_1$. After the first bifurcation, the channel collecting most of the fluid injected at Q_0 is labeled Branch 0 and the other channel is referred to as Branch 1. A binary notation system is later introduced to identify high-order branches. We first examine thread morphology in the central channel and the conditions required to direct a thread in distributary channels.

3 Lateral position and size of threads

Hydrodynamic control of viscous miscible fluid interfaces is readily achieved using laminar flow properties of microscale flows. Experiments are carried out to interrogate the relationship between thread location y_T and size ε with the symmetry ratio $\varphi_S = Q_0/Q_1$ and the absolute flow rate ratio $\varphi_0 = Q_A/Q_B$ (Fig. 2a). For each set of experiments, the total side flow rate $Q_B = Q_0 + Q_1$ is kept constant while Q_0 and Q_1 are modified to modulate φ_S for a given Q_A. Measurements are carried out a few channel diameters away from the junction at $x/h \sim 5$ when the thread has reached its final position in the central channel (Fig. 2b). For thin threads when $Q_A \ll Q_B$, the viscous filament is expected to be located at the virtual interface formed by the side injections in the main channel (Fig. 2a—inset). To illustrate this type of operating conditions at low $Re \sim O(1)$, Q_B is set to 200 μL/min and the influence of φ_S on thread behavior is examined for various $Q_A = 1$, 2, 5, 10, 20, and 50 μL/min.

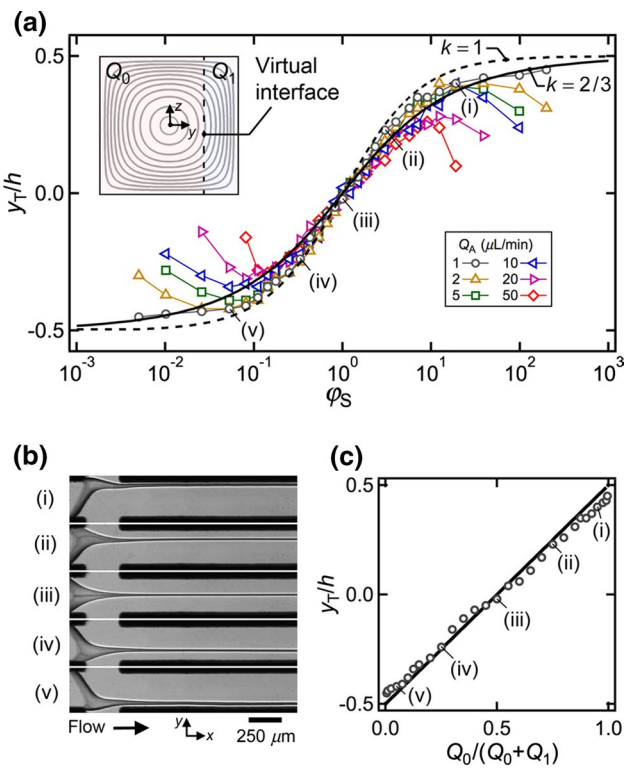

Fig. 2 Lateral thread positioning controlled with side flow rates Q_0 and Q_1 for $\chi = 180$. Flow rates are expressed in μL/min. **a** Evolution of thread lateral position y_T as a function of symmetry ratio $\varphi_S = Q_0/Q_1$ for a fixed sheath flow rate $Q_0 + Q_1 = 200$ and various thread flow rates Q_A. *Solid* and *dash lines* $y_T/h = (1 + \varphi_S^{-k})^{-1} - 0.5$. **b** Micrographs showing the production of small off-centered threads in the focusing section for $Q_A = 1$ and $(Q_0, Q_1) = (i)$ (190, 10), (ii) (50, 150), (iii) (100, 100), (iv) (150, 50), and (v) (10, 190). **c** Evolution of thread position versus side flow rate fraction for $Q_A = 1$. *Solid line* $y_T = Q_0/(Q_0 + Q_1) - 0.5$

In purely laminar flow conditions, the position of the virtual interface between the two side flows is computed by integrating the Fourier series describing the velocity profile in a square duct (White 1991) and expressed as a function of φ_0 to obtain a 'S-curve.' Using a parallel-plate approximation with a flat interface between sheath streams having identical viscosity η_B, a simple analytical solution can be expressed according to

$$y_T/h = \left(1 + \varphi_S^{-k}\right)^{-1} - 0.5, \tag{1}$$

with the coefficient $k = 1$ (Cubaud and Mason 2008). In practice, the coefficient k controls the steepness of the curve, and when $k = 2/3$, the curve is found to closely follow that of the computed solution for the virtual interface between two side streams with <1 % variation from the ideal curve. This method allows us to employ a simple analytical expression to approximate the theoretical interface location calculated through direct velocity profile integration. We find experimentally that most data points are located between the curves defined with $k = 1$ and 2/3 (Fig. 2a). While the influence of φ_0 is relatively negligible when φ_S ranges between 10^{-1} and 10^{1}, each curve displays end tails departing from the basic curve as φ_0 is increased due a swelling of thread near the sidewalls and the possibility of partial thread lubrication, i.e., threads not fully detached from the top and bottom walls similar to the tubing regime in square

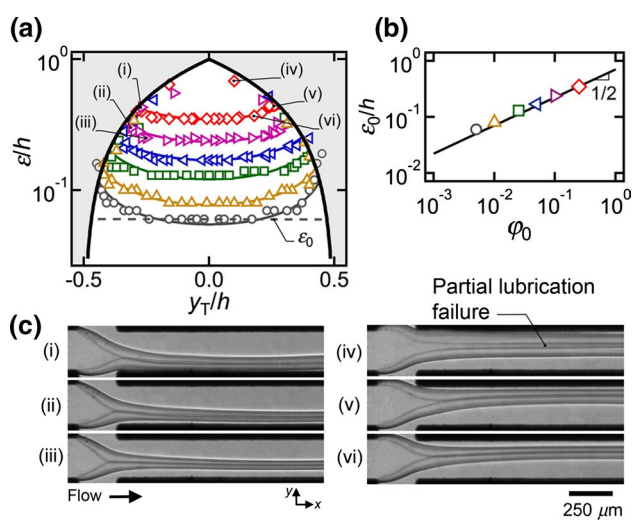

Fig. 3 Size of off-centered threads in the main channel. Flow rates are expressed in μL/min, $\chi = 180$. **a** Evolution of normalized thread diameter ε/h as a function of lateral position y_T/h for various central flow rates $Q_A = 1$, 2, 5, 10, 20, 50 (from *bottom* to *top*), see text for details. **b** Measurement of central thread diameter ε_0 as a function of φ_0, *solid line* $\varepsilon_0/h = (\varphi_0/2)^{1/2}$. **c** Experimental micrographs for threads near sidewalls, $Q_A = 20$ and $(Q_0, Q_1) = (i)$ (10, 190), (ii) (15, 185), and (iii) (50, 150); $Q_A = 50$ and $(Q_0, Q_1) = (iv)$ (185, 15), (v) (180, 20), and (vi) (160, 40)

channels (Cubaud and Notaro 2014) or plane microfluidic chambers (Darvishi and Cubaud 2011). Incidentally, in this series of experiments, an intriguing property arises for fixed $Q_B = Q_0 + Q_1$, where the thread location is a linear function of one normalized side flow rate according to $y_T \approx Q_0/(Q_0 + Q_1) - 0.5$ (Fig. 2c). The previous expression can be directly deduced from the parallel-plate approximation for $k = 1$ and gives excellent result when φ_S is near unity. However, in the following we elect to use the coefficient $k = 2/3$ as it yields better estimate for the thread location for small and large φ_S.

The correlation between the thread lateral position and size in the central channel is shown in Fig. 3a. The swelling of threads near the sidewalls can be described using mass conservation and assuming plug flow for the viscous thread, i.e., uniform velocity profile within the thread, in the low-velocity regions of the sheath fluid near solid boundaries. The gray area in the graph corresponds to regions in the parameter space where the thread size would be larger than the distance from the sidewalls, which is simply defined with $\varepsilon/2 = 0.5 - y_T$ for $y_T > 0$ and $\varepsilon/2 = 0.5 + y_T$ for $y_T < 0$. Experiments conducted for various Q_A are in good accordance with this argument. For large thread sizes, near the no-zone limit, the shift in position toward the center of the channel is due to a partial lubrication failure, i.e., the central part of the thread does not fully detach from the top and bottom walls. The thread bistability is more pronounced for large thread size, which corresponds to large Q_A (Fig. 3c). A useful approximation for the functional relationship between small thread size ε and y_T can be deduced analytically assuming a cylindrical thread in plug flow according to

$$\pi\varepsilon^2/4 = Q_A/U, \tag{2}$$

where U is the local velocity deduced from the nearly parabolic profile of the sheath fluid in the median plane of the square channel,

$$U = 2.1 J_{Tot}\left(1 - 4\left[y_T/h\right]^2\right), \tag{3}$$

with the total multiphase flow superficial velocity $J_{Tot} = (Q_A + Q_0 + Q_1)/h^2$. Combining Eqs. 2 and 3 to express ε as a function of y_T yields good agreement with experimental data, and a nearly constant thread size ε_0 is measured near the channel central line at $y_T \approx 0$ (Fig. 3a). As expected, the central thread size follows the scaling law $\varepsilon_0/h = \alpha_S \varphi_0^{1/2}$ with a prefactor $\alpha_S = 2^{-1/2}$ (Cubaud and Notaro 2014) for large viscosity contrast $\chi \gg 1$ (Fig. 3b). Overall, the thread size and location are found relatively independent of the viscosity contrast χ, which allows us to finely control thread positioning and size in the central channel and examine in detail the dynamic thread response to the first bifurcation.

4 Phase diagram in branching channels

The specific branching geometry investigated in this work where a single channel separates into two channels of equal size results in a flow deceleration, which can initiate viscous buckling instabilities depending on fluid properties and flow parameters. Here, we systematically examine thread behavior in the first bifurcation between main and secondary channels. The observed flow patterns consist of (1) thread folding on the splitting edge for symmetry ratios φ_S near unity, (2) thread transport in secondary channels for small and off-centered threads, and (3) fouling of secondary channel for large threads near sidewalls. A typical phase diagram with corresponding flow patterns is shown in Fig. 4 where the absolute flow rate ratio φ_0 is expressed as a function of the symmetry ratio φ_S. The transition lines between transport and folding regimes are calculated for $A/2 \sim |y_T|$, where A is the folding amplitude. Previous work has shown that A is essentially proportional to the thread size ε with a coefficient that depends on the

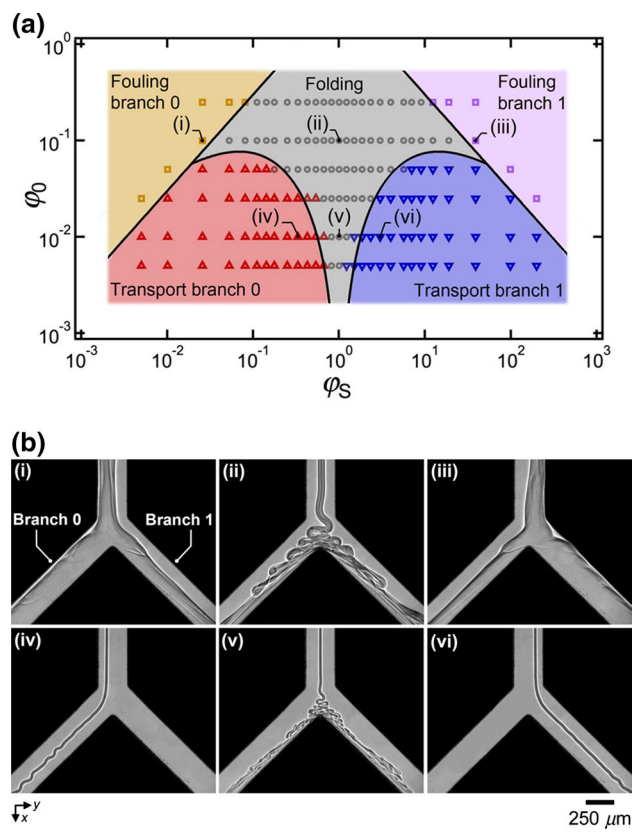

Fig. 4 **a** Phase diagram of viscous threads behavior in branching microchannels based on absolute flow rate ratio φ_0 and symmetry ratio φs for constant $Q_B = 200$ μL/min and viscosity contrast $\chi = 180$. Transition lines between folding and transport regimes are calculated using Eq. (4). **b** Experimental micrographs of thread regimes with corresponding flow rates in μL/min, $(Q_A, Q_0, Q_1) = (i)$ (20, 5, 195), (*ii*) (20, 100, 100), (*iii*) (20, 195, 5), (*iv*) (2, 50, 150), (*v*) (2, 100, 100), and (*vi*) (2, 150, 50)

viscosity contrast χ and the microchannel geometry (Cubaud et al. 2011). Here, experiments suggest that $A \approx 2.4\varepsilon$ and this finding is used in conjunction with Eqs. 2 and 3 to express the condition for a folded thread to intercept the splitting edge of the bifurcation ($A/2 \sim |y_T|$) such as:

$$c(y_T/h)^2\left[1-4(y_T/h)^2\right] \sim \left(1+\varphi_0^{-1}\right)^{-1}, \quad (4)$$

where the constant $c \approx 1.14$ is calculated from geometric parameters and folding amplitude, and y_T is expressed using Eq. 1 with $k = 2/3$. Solving for the direct relationship between φ_0 and φ_S yields a rather cumbersome expression involving ratios of polynomial functions, which is more conveniently represented graphically in Fig. 4. This criterion for the folding/transport transition shows good agreement with experimental data for small and large φ_S. Conversely, the use of $k = 1$ for relating y_T and φ_0 allows for more finely matching experimental data when the symmetry ratio is near unity with transition lines for positive and negative y_T coming closer to one another. The fouling transition is reached when the thread is near the sidewalls and displays partial lubrication, which corresponds to a similar criterion as previously used, specifically $\varepsilon/2 = 0.5 - y_T$ for $y_T > 0$ and $\varepsilon/2 = 0.5 + y_T$ for $y_T < 0$ and we find $\varphi_0 \sim 3\varphi_S$ for $\varphi_S \ll 1$ and $\varphi_0 \sim 3/\varphi_S$ for $\varphi_S \gg 1$. The rich dynamical behavior of the threads at a bifurcation can be utilized to produce lubricated threads or complex stratifications in branching channels. In particular, the presence of a spatially fixed splitting edge is useful for better understanding how the folding frequency f of a thread is related to viscosity contrasts and local flow velocities.

5 Folding instability

In this section, we examine the viscous buckling behavior of a thread directly impinging the solid edge of the bifurcation. The folding frequency f is measured at the bifurcation for different fluid pairs (Fig. 5). A spatiotemporal diagram is created from high-speed movies generated for each flow rate and fluid pair to compute the average folding period $T = f^{-1}$ (Fig. 5b—inset). In general, we find that large threads display a regular folding mechanism where each fold is alternatively deposited into each branching channel. By contrast, small threads can adopt a more complex behavior with the alternate deposition of two folds in each branching channel. Overall, the folding frequency appears to be relatively independent of the deposition mode since it is controlled through upstream condition in the square channel. As the thread is convected at velocity U toward the channel edge, the folding frequency should scale as $f \sim U/S$ where S is the arc length of a fold. Previous work (Cubaud et al. 2011) conducted on the shape of folded threads made of similar

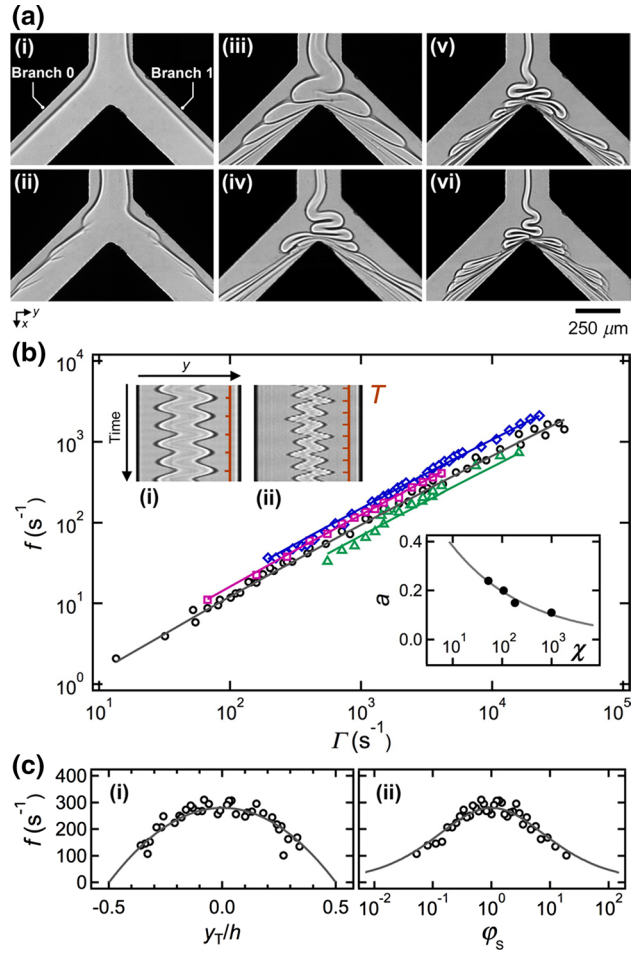

Fig. 5 Viscous thread folding in branching microchannels. **a** Micrographs of central folding, from stagnation flow to multistate folding, $\chi = 52$, $\varphi_S = 1$, $\varphi_0^{-1} =$ (*i*) 1, (*ii*) 1.5, (*iii*) 2, (*iv*) 6, (*v*) 9, and (*vi*) 14. **b** Folding frequency f versus buckling rate Γ for viscosity contrast $\chi = 52$ (*open diamond*), 106 (*open square*), 180 (*open circle*), and 990 (*open triangle*), *solid lines* $f = a\Gamma^k$, with exponent $k = \Gamma^{-0.01}$ and coefficient $a = 0.7\chi^{-0.28}$ (*inset right*). *Inset left* spatiotemporal diagrams used to calculate the folding period T during simple and complex thread deposition into secondary channels. **c** Evolution of folding frequency f versus (*i*) thread location y_T and (*ii*) symmetry ratio φ_s for $\chi = 190$, $Q_A = 10$ and $Q_B = 200$ μL/min; *solid lines* correspond to $f = f_0\,(1 - 4[y_T/h]^2)$, where f_0 is the average frequency at $y_T = 0$

fluids in microchannels has shown that the arc-to-wavelength ratio λ/S weakly increases with χ and the wavelength remains proportional to the folding amplitude, $\lambda \propto A$, for moderate values of the viscosity contrast. Hence, the proportionality between the folding amplitude and the thread diameter, $A \propto \varepsilon$, suggests that the arc length S scales with ε. Therefore, for each fluid pair investigated in this study, we calculate the effective rate of buckling according to

$$\Gamma = U/\varepsilon. \quad (5)$$

The evolution of the folding frequency f is shown as a function of Γ in Fig. 5b for various χ. As the viscosity contrast is varied, data points fall into curves that appear parallel to one another and are fitted with a scaling law $f = a\Gamma^k$, where the exponent $k = \Gamma^{-0.01}$ slightly decreases from unity as the flow velocity increases and the coefficient $a = 0.7\chi^{-0.28}$ is a weak function of the viscosity contrast. This finding essentially corroborates early work related to viscous folding in diverging microchannels (Cubaud and Mason 2006) where, similar to the viscous regime in large-scale experiments of sheet folding and thread coiling (Ribe 2003; Maleki et al. 2004; Ribe et al. 2012), f was found proportional to the flow velocity in the viscous regime. In this work, we obtain a more refined microfluidic measurement of f, which allows us to clarify the thread folding behavior in relation to flow structure and fluid composition. The presence of a varying exponent k suggests a possible small non-Newtonian structural behavior of the polymeric oil used to form the thread in the experiment at large shear rate. This aspect, which is beyond the scope of the present work, would be worth examining using strongly non-Newtonian fluids in future studies.

The additional degree of control offered through experimentally dissociating side flow rates and using the symmetry ratio φ_S also permits to measure f for threads positioned at different locations in the parabolic velocity profile of the central channel. In this case, we employ a methodology similar to the one used before, namely fixing φ_0 with constant Q_A and Q_B to obtain a constant total multiphase flow superficial velocity J_{Tot} and varying the symmetry ratio φ_S. Owing to small variations for f at different locations, results show that the folding frequency is indeed proportional to the local flow velocity of the sheath fluid near the thread in the parabolic flow profile (Fig. 5c).

6 Thread dynamics in networks

We now turn our attention to the evolution of miscible fluid threads in the transport regime in secondary channels and beyond along the multiple branching channel geometry. The flow evolution is monitored along multiple bifurcations of square microchannels of identical width h. Figure 6 shows the binary notation system used to label various regions of the network. We denote by N the bifurcation number and use a binary code for addressing various branch names, such as Branch 00 for a tertiary channel and Branch 000 for a quaternary channel along the network. Our specific geometrical constrain imposes a sheath flow rate of per branch according to $Q_B/2^N$. Therefore, after three nodes, one obtains a flow rate reduction per channel of $Q_B/8$, which can induce significant thread swelling due to the localized increase of φ_0 and results in the development of complex thread morphologies and viscous stratifications. Although the bifurcation angle remains equal to $\pi/2$ throughout the network, the incidence angle made between a feeding channel and distributaries is $\pi/2$ for the first bifurcation ($N = 1$) and $\pi/4$ for second and third bifurcations ($N = 2$ and 3). Assuming purely laminar flow conditions and a negligible influence of the thread flow rate for $Q_A \ll Q_B$, the stagnation streamlines separating distributaries can be calculated for the sheath flow using Eq. (1). Given the increasingly large range of parameter space associated with the complete exploration of the system, here we discuss the phenomenology of a few typical flow processes for threads and stratifications observed during the course of this investigation.

We first examine the evolution of viscous miscible fluid threads in various branches of the system. In addition to the folding instability of viscous threads in decelerating flows, which typically occurs at bifurcations, a shear-induced

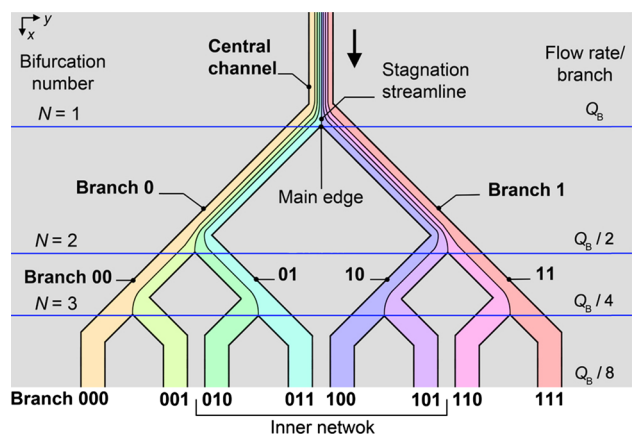

Fig. 6 Schematic representation of dichotomous distributary microfluidic array composed of a binary network made of square microchannels of identical width

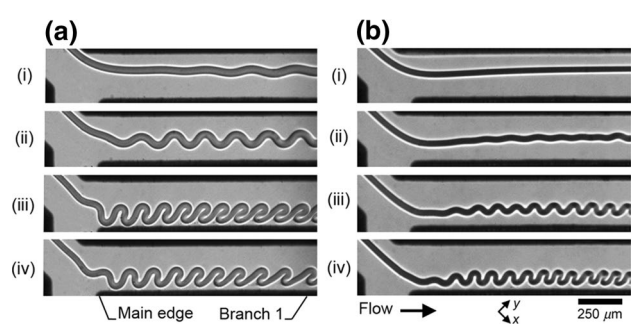

Fig. 7 Example of thread morphology in the transport regime in a secondary channel (Branch 1). **a** Moderate viscosity contrast, $\chi = 180$, $\varphi_0 = 2.5 \times 10^{-2}$, $\varphi_S =$ (*i*) 9, (*ii*) 5.7, (*iii*) 4, and (*iv*) 3. **b** Large viscosity contrast, $\chi = 990$, $\varphi_0 = 10^{-2}$, $\varphi_S =$ (*i*) 4, (*ii*) 3, (*iii*) 2.3, and (*iv*) 1.9

buckling instability—previously labeled as swirling instability (Cubaud and Mason 2012)—can also develop along a straight channel and can significantly deform threads located in the high shear region of the sheath fluid near the sidewalls. Given the relatively short length of the central channel, which is used to position threads, significant thread deformations are only observed in secondary channels and beyond in the transport regime. The combination of folding and swirling instabilities produces intricate thread undulations (Fig. 7). An important consequence of the branching geometry is the shift in the streamlines position from a channel to another, which modifies thread lateral position in different branches. Indeed, in the asymptotic limit of equal distribution of sheath fluid in each branch for $Q_A \ll Q_B$, streamlines are expected to shift toward the center of the channel to maintain local mass conservation. This hydrodynamic property tends to displace threads near the channel centerline and reduces the influence of the swirling effect due to sidewalls, which is advantageous for thread transport stability. As can be seen in Fig. 7, sinuous perturbations develop along various threads with asymmetrical distortions near sidewalls. This ability of a thread to sustain viscous buckling instabilities as well as bending resistance in confined microfluidic systems increases with thread size ε and viscosity contrast χ.

A range of thread behaviors is observed depending on fluid and flow properties. The system allows for directing threads into the network and permits the capture of emerging phenomena depending on thread history across the fluidic network. For instance, for low-viscosity contrasts, a thin thread near a wall can rupture into swirls as a result of shear produced by the sheath fluid. As such structures evolve, they adopt different shapes that become more compact after bifurcation since the reduction in the flow rate in each channel produces a compressive stress on slender structures (Fig. 8a-i). Other examples consist of a thread undergoing a complex path in the network (Fig. 8a-ii) and the folding of a shear-deformed thread at a second bifurcation (Fig. 8a-iii). For moderate viscosity contrasts, strong buckling deformation limits the manipulation of large threads and produces complex morphologies. For instance, Fig. 8b-i, b-ii shows the interaction between thread size and location in microgeometries, and Fig. 8b-iii shows a folded thread impinging another bifurcation. In general, we find that the prediction of thread location in the network is more accurate for branches in the inner network—near the projection of the central channel—due to ease in manipulating thread location and size near the central axis. Overall, the morphologies observed are somewhat reminiscent of geological features, such as folded veins in rocks (Johnson and Fletcher 1994) and enclaves in lava flows (Manga and Ventura 2005) .

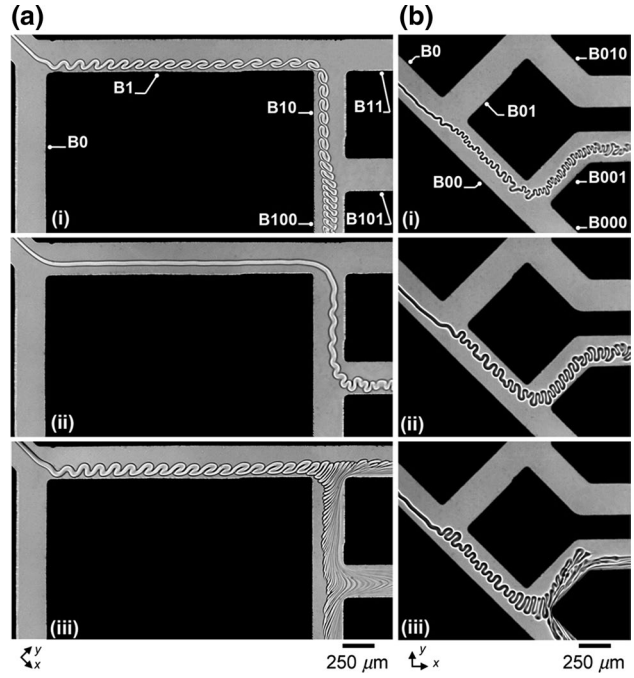

Fig. 8 Examples of thread evolution in network with formation of complex substructures. **a** Small viscosity contrast $\chi = 52$, (Q_A, Q_0, Q_1) = (*i*) (5, 120, 80), (*ii*) (5, 140, 60), and (*iii*) (50, 260, 700). **b** Moderate viscosity contrast $\chi = 180$, (Q_A, Q_0, Q_1) = (*i*) (1, 30, 170), (*ii*) (2, 30, 170), and (*iii*) (2, 20, 180)

7 Formation and evolution of heterogeneous viscous stratifications

Another important aspect of thread separation in branching channels is the formation of stratifications. The folding instability provides a natural mean to enhance the specific area between low- and high-viscosity fluids and produces spatially evolving stratifications made of folded threads. Here, we examine the flow produced in secondary channels as a result of thread folding instability. Given the complexity associated with this type of flows, we restrict our analysis to threads that are initially centered in the main channel, i.e., for a symmetry ratio $\varphi_S = 1$. The viscous fluid deposition mechanism and the resulting stratifications strongly depend on the viscosity ratio χ and absolute flow rate ratio φ_0. Figure 9 shows strata obtained for small and large viscosity contrasts. For low χ, the thread folding amplitude is relatively small and regular flow patterns are produced, while increasing complex flows are obtained when χ is large. For large φ_0, stratifications do not significantly differ from a homogeneous stratification with simple fluid arrangement. Indeed, geometrical confinement of partial lubricated threads restricts strong thread folding; however, as the thread size decreases, folding lines are included in the strata. The average velocity profile in the strata

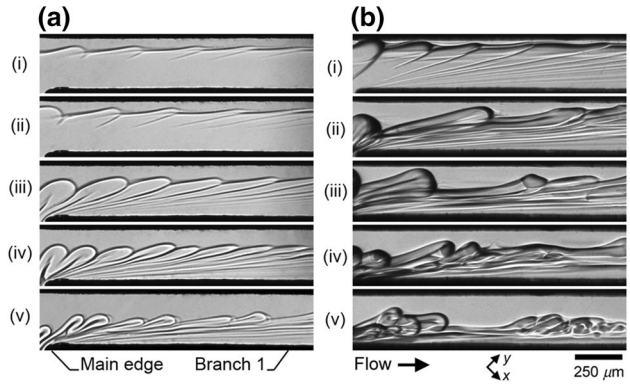

Fig. 9 Formation of complex stratifications in a secondary channel (Branch 1) for $\varphi_s = 1$. **a** Foliated strata for low-viscosity contrast $\chi = 52$, $\varphi_0^{-1} =$ (*i*) 1.5, (*ii*) 1.7, (*iii*) 2.5, (*iv*) 4.5, and (*v*) 11. **b** Heterogeneous strata for large viscosity contrast $\chi = 990$, $\varphi_0^{-1} =$ (*i*) 2.7, (*ii*) 4, (*iii*) 4.5, (*iv*) 13, and (*v*) 20

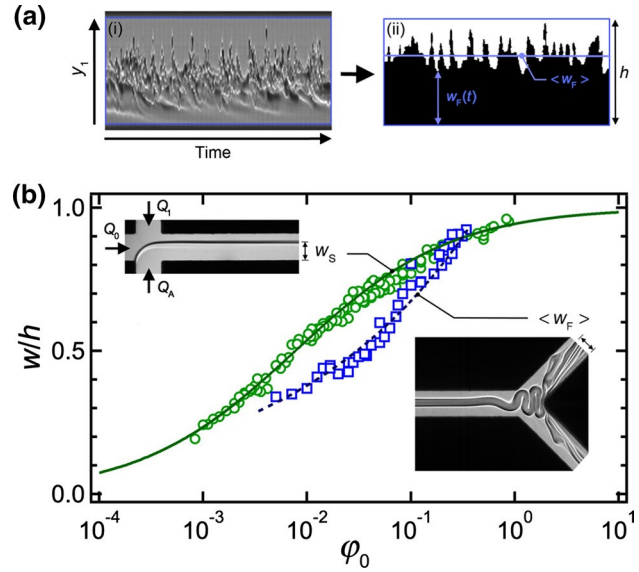

Fig. 10 Width of stratifications for large viscosity contrasts $\chi = 990$. **a** Estimation of time-average width $<w_F>$ for $\varphi_0^{-1} = 20$ at fixed location in Branch 1 using spatiotemporal analysis, (*i*) raw diagram, (*ii*) processed diagram. **b** Variation in width as a function of φ_0 for simple strata, w_S (*open circle*), and for strata formed by thread folding, $<w_F>$ (*open square*). *Solid line* $w_S/h = [1 + [130\ \varphi_0]^{-0.58}]^{-1}$, *dash line* $<w_F>/h = 1.2\varphi_0^{1/4}$

appears to be quasi-linear as fold lines are stretched into straight line anchored to the bifurcation edge. A large shear is exerted at the strata interface by the fast, low-viscosity stream. The increase in the spacing between striations produced by fold lines along the flow direction indicates flow acceleration.

To better understand the role of the folding instability on the morphology and dynamic of stratifications resulting from thread contact with solid walls, we measure the time-averaged width $<w_f>$ of fluid deposition onto the inside walls of secondary channels for large viscosity contrast $\chi = 990$. To this end, we produce spatiotemporal diagrams using the reslice function in *ImageJ*[1] applied to a segment that is normal to the local channel axis, which creates a composite image where the instantaneous width w_f appears in the *y*-axis and each time frame is shown in the *x*-axis (Fig. 10a). Each diagram is treated using a series of filters to create a binary image from which $<w_f>$ can be computed. Images are taken from high-speed movies and typically cover at least a decade of folding periods $T = 1/f$ to compute representative averages. For comparison, we also plot the width w_s of a simple stratification produced using the same fluid pair. In this case, the initial injection scheme is modified to inject the high-viscosity fluid L_A from a side channel at Q_A and the low-viscosity fluid L_B from the other side channel and the central channel as shown in the upper inset of Fig. 10b. Assuming equal distribution in each branch, the absolute flow rate ratio φ_0 is expected to remain the same before and after the bifurcation for $\varphi_S = 1$, which allows for a direct comparison between simple and complex stratifications. Data for the single strata configuration are fitted using a variant of Eq. 1 with an exponent $k = 0.58$ along with a coefficient depending on the viscosity contrast χ,, and average width measurements of complex stratifications are correlated with φ_0 using a scaling law (Fig. 10b). Overall, we find that $<w_f>$ is typically less than w_s for φ_0 ranging between 10^{-2} and 10^{-1}. Using a simple mass conservation argument based the average stratification velocity $V = Q_A/(h < w_f >)$, this behavior suggests an enhanced transport of viscous material when deposited on the walls through folding compared to a bulk channel fluid injection. As a large difference in average velocities is observed between stratified and lubricated flows, complex stratifications formed through the deposition of a lubricated thread adopt an intermediate behavior.

The formation of intricate, pseudo-chaotic stratifications in laminar flow conditions offers the possibility to examine the evolution of viscous composite flows in dichotomous networks for large viscosity contrasts χ. In particular, evolving stratifications made of folded viscous filaments can foul high-order channels depending on the absolute flow rate ratio φ_0. As φ_0 increases, channels in the inner network become progressively 'jammed' with the high-viscosity fluid (Fig. 11a). This mechanism directly results from the large difference in frictional pressure drop due to the viscosity coefficient η of each fluid and drastically raises the fluidic resistance of channels filled with the high-viscosity fluid. Once a channel is fouled, minute quantities of the low-viscosity fluid, which are initially trapped by fold

[1] ImageJ. http://rsb.info.nih.gov/ij/.

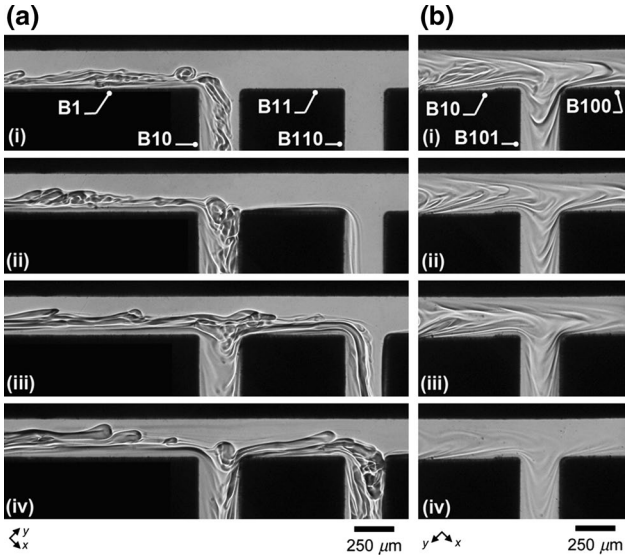

Fig. 11 Evolution of complex strata in branching network for $\varphi_S = 1$ and $\chi = 990$. **a** Fouling of tertiary and quaternary channels for various flow rate ratios $\varphi_0^{-1} =$ (*i*) 40, (*ii*) 27, (*iii*) 20, and (*iv*) 13. **b** Formation of chevron-like structures in fouled branches $\varphi_0^{-1} =$ (*i*) 5.3, (*ii*) 4.5, (*iii*) 3.7, and (*iv*) 1.6

lines, can enter a slow-moving jammed branch and produce typical chevron-like structures (Fig. 11b). This behavior is observed after the second bifurcation and is accentuated in high-order distributaries, suggesting the possibility to blend small proportions of low-viscosity fluids with high-viscosity fluids.

8 Conclusions

In this article, we characterize the behavior of threads made of high-viscosity fluids flowing in a sheath of miscible, low-viscosity fluids in a splitting microfluidic network. We first discuss the influence of fluid injection scheme and flow rates on the position y_t and size ε of threads in the main square microchannel and develop analytical expressions for finely controlling viscous filament trajectories and dimensions. A phase diagram detailing the various flow patterns observed at the first node is presented based on the absolute flow rate ratio φ_0 and symmetry ratio φ_S with the identification of three main regimes, including thread folding, fouling, and transport. We then study the folding instability of a centered thread impinging the edge of the first bifurcation along with the influence of the local velocity field on the folding frequency f. The evolution of high-viscosity core-annular flows is also examined in distributaries with focus on thread deformation along various sections of the system. We finally investigate the structural arrangement of fluids in the inner network for the case of stratifications made from a folded thread, and we describe the mechanism of viscous jamming along with the formation of chevron-like structures, which indicate a degree of mixing between different low- and high-viscosity components.

The microfluidic regimes analyzed in this work display very rich dynamics. Although complete characterization of high-viscosity multiphase flows in branching networks is beyond the scope of the present investigation, we shed light on a few basic properties of lubricated and stratified flows that could serve as a basis for the development of in-line mixing methods with thick materials in small fluidic passages. We show, in particular, that geometrical confinement of viscous buckling instabilities can be utilized to increase the interfacial area between viscosity-differing fluids and produce heterogeneous flows at the small scale. Better understanding transitions between lubricated and stratified flows and the associated disparity in residence times between species in each stream is pivotal for improving the flow management of highly viscous materials in microgeometries. To further characterize such phenomena in separating channels, future investigations could focus on the influence of the slipping angle on thread bending and folding and the role of various aspect ratios between distributaries to manipulate streamlines and local convective accelerations. Potential extensions of this work also include the use of non-Newtonian fluids as well as immiscible fluid pairs along with the study of threads behavior during inertial or diffusive instabilities, which, respectively, occur for large and low injection rates of miscible fluids. Overall, this study opens up a range of new microfluidic designs for the manipulation of viscous threads, and the observation of phenomena reminiscent of large-scale viscous flows found in the environment offers the intriguing perspective of the realization of geological labs on chips using appropriate similitude approaches.

Acknowledgments We have appreciated discussions with Neil Ribe and Damir Juric. This material is based on work supported by the National Science Foundation under Grant No. CBET-1150389.

References

Barnett CH, Cochrane W (1956) Flow of viscous liquids in branched tubes-with reference to the hepatic portal vein. Nature 177:740–742

Brouzes E, Kruse T, Kimmerling R, Strey H (2015) Rapid and continuous magnetic separation in droplet microfluidic devices. Lab Chip 15:908

Cao Q, Ventresca AL, Sreenivas KR, Prasad AK (2003) Instability due to viscosity stratification downstream of a centerline injector. Can J Chem Eng 81:913–922

Couper JR, Penney WR, Fair JR, Walas SM (2005) Chemical process equipment: selection and design. Elsevier Inc., Oxford

Cubaud T, Mason TG (2006) Folding of viscous threads in diverging microchannels. Phys Rev Lett 96:114501

Cubaud T, Mason TG (2008) Formation of miscible fluid microstructures by hydrodynamic focusing in plane geometries. Phys Rev E 78:056308
Cubaud T, Mason TG (2012) Interacting viscous instabilities in microfluidic systems. Soft Matter 8:10573
Cubaud T, Notaro S (2014) Regimes of miscible fluid thread formation in microfluidic focusing sections. Phys Fluids 26:122005
Cubaud T, Jose BM, Darvishi S (2011) Folded micro-threads: role of viscosity and interfacial tension. Phys Fluids 23:042002
Darvishi S, Cubaud T (2011) Lubrication of highly viscous core-annular flows in microfluidic chambers. J Fluids Eng 133:031203
Engl W, Roche M, Colin A, Panizza P, Ajdari A (2005) Droplet traffic at a simple junction at low capillary numbers. Phys Rev Lett 95:208304
Engl W, Ohata K, Guillot P, Colin A, Panizza P (2006) Selection of two-phase flow patterns at a simple junction in microfluidic devices. Phys Rev Lett 96:134505
Guillot P, Panizza P, Salmon JB, Joanicot M, Colin A, Bruneau CH, Colin T (2006) Viscosimeter on a microfluidic chip. Langmuir 22:6438
Hardt S, Hahn T (2012) Microfluidics with aqueous two-phase systems. Lab Chip 12:434
Johnson AM, Fletcher RC (1994) Folding of viscous layers. Columbia University Press, New York
Joseph DD, Nguyen K, Beavers GS (1984) Non-uniqueness and stability of the configuration of flow of immiscible fluids with different viscosities. J Fluid Mech 141:319–345
Jullien M-C, Tsang Mui Ching M-J, Cohen C, Menetrier L, Tabeling P (2009) Droplet breakup in microfluidic T-junctions at small capillary numbers. Phys Fluids 21:072001
Lenshof A, Laurell T (2010) Continuous separation of cells and particles in microfluidic systems. Lab Chip 39:1203–1217
Leshansky AM, Afkhami S, Jullien M-C, Tabeling P (2012) Obstructed breakup of slender drops in a microfluidic T junction. Phys Rev Lett 108:264502
Link DR, Anna SL, Weitz DA, Stone HA (2004) Geometrically mediated breakup of drops in microfluidic devices. Phys Rev Lett 92:054503
Madou MJ (2012) Fundamentals of macrofabrication and nanotechnology, vol II. CRC Press, Boca Raton
Maleki M, Habibi M, Golestanian R, Ribe NM, Bonn D (2004) Liquid rope coiling on a solid surface. Phys Rev Lett 93:214502
Manga M, Ventura G (2005) Kinematics and dynamics of lava flows. The Geological Society of America Inc, Boulder, CO
Ménétrier-Deremble L, Tabeling P (2006) Droplet breakup in microfluidic junctions of arbitrary angles. Phys Rev E 74:035303(R)
Parthiban P, Khan SA (2013) Bistability in droplet traffic at asymmetric microfluidic junctions. Biomicrofluidics 7:044123
Pozrikidis C (2012) Passage of a liquid drop through a bifurcation. Eng Anal Bound Elem 36:93–103
Ribe NM (2003) Periodic folding of viscous sheets. Phys Rev E 68:036305
Ribe NM, Habibi M, Bonn D (2012) Liquid rope coiling. Annu Rev Fluid Mech 44:249
Tritton DJ (1988) Physical fluid dynamics. Oxford University Press Inc., New York
White FM (1991) Viscous fluid flow. McGraw-Hill, New York
Xia HM, Wang ZP, Koh YX, May KT (2010) A microfluidic mixer with self-excited 'turbulent' fluid motion for wide viscosity ratio applications. Lab Chip 10:1712